UC Irvine
UC Irvine Previously Published Works

Title

Quantitative magnetization transfer MRI of desmoplasia in pancreatic ductal adenocarcinoma xenografts.

Permalink

https://escholarship.org/uc/item/2rh160xt

Journal

NMR in biomedicine, 26(12)

ISSN

0952-3480

Authors

Li, Weiguo
Zhang, Zhuoli
Nicolai, Jodi
et al.

Publication Date

2013-12-01

DOI

10.1002/nbm.3004

Peer reviewed

Quantitative Magnetization Transfer MRI of Desmoplasia in Pancreatic Ductal Adenocarcinoma Xenografts

Weiguo Li[1], **Zhuoli Zhang**[1,2], **Jodi Nicolai**[1], **Guang-Yu Yang**[2,3], **Reed A. Omary**[1,2,4], and **Andrew C. Larson**[1,2,4]

[1]Department of Radiology, Feinberg School of Medicine, Northwestern University, Chicago, Illinois, USA

[2]Robert H. Lurie Comprehensive Cancer Center, Northwestern University, Chicago, Illinois, USA

[3]Department of Pathology, Northwestern University, Chicago, IL, 60611, USA

[4]Department of Biomedical Engineering, Northwestern University, Evanston, Illinois, USA

Abstract

Quantitative assessment of desmoplasia in pancreatic ductal adenocarcinoma (PDAC) may be critical for staging or prediction of response to therapy. We performed quantitative magnetization transfer (qMT) MRI measurements in 18 mouse xenograft tumors generated from 3 PDAC cell lines. The qMT parameter, bound proton fraction (BPF), was found to be significantly higher in tumors grown using the BxPC-3 cell line (5.31 ± 0.87, mean $\pm$ standard deviation) compared to the BPF measured for tumors grown from Panc-1 (3.65 ± 0.60) and Capan-1 (1.50 ± 0.58) cell lines ($P < 0.05$ for each comparison). Histologic measurements demonstrated a similar trend; BxPC-3 tumors had significantly higher fibrosis levels (percentage of fibrotic tissue area, 6.21 ± 2.10) compared to Panc-1 (2.88 ± 1.13) and Capan-1 (1.69 ± 1.01) tumors. BPF was well correlated to quantitative fibrosis levels ($r = 0.77$, $P < 0.01$). Our results indicate that qMT measurements offer the potential to noninvasively quantify fibrosis levels in PDAC mouse xenograft models and thus serve as a valuable *in vivo* biomarker of desmoplasia in PDAC.

Keywords

Quantitative Magnetization Transfer; Bound Proton Fraction; desmoplasia; Pancreatic Cancer; Xenograft

Introduction

Pancreatic ductal adenocarcinoma (PDAC) is one of the most lethal human malignancies. PDAC is highly aggressive with no systemic therapies available for effective treatment of patients with advanced disease (1). Desmoplasia leads to the formation of a fibrotic fortress-like hypovascular barrier that surrounds PDAC and impairs the delivery of chemotherapeutics (2). Quantitative measurements of fibrosis levels in PDAC may be highly valuable for disease staging, selection of optimal therapies and/or prediction or monitoring of therapeutic outcomes. However, biopsy—the current gold standard for histologic assessment tissue desmoplasia—has several limitations, such as sampling error, intra- and

Please send proof and correspondence to: **Andrew C. Larson**, Department of Radiology, Feinberg School of Medicine, Northwestern University, 737 N. Michigan Ave, 16th Floor, Chicago, IL 60611, Phone: (312)926-3499, Fax: (312)926-5991, a-larson@northwestern.edu.

inter-observer variability, and the potential for complications given the invasive nature of the procedure.

As a non-invasive and non-ionizing imaging modality, magnetic resonance imaging (MRI) can be useful for the evaluation of PDAC desmoplasia using various different contrast mechanisms such as diffusion-weighted MRI (3-5), dynamic contrast enhanced MRI (6), and recently magnetization transfer (MT) MRI (7). MT MRI provides unique image contrast for the characterization of tissues beyond conventional T_1, T_2, and T_2 * weighting for a variety of different clinical applications (8,9). Physically, MT is a dynamic process involving the exchange of magnetization between sub-populations of free water protons and those water protons bound to macromolecules (8,10). These binding protons cannot be observed directly with conventional MRI methods because of their extremely short T_2 relaxation times ($T_2 \sim 10$ μs). However, saturation of the macromolecular protons indirectly affects the observable MR signal from free water protons through the exchange of magnetization. Macromolecular composition can vary widely between different tissues and disease states and MRI scans sensitized to the MT phenomenon can thus produce images with strong signal contrast between these tissues.

The magnetization transfer ratio (MTR) calculated from typical MT MRI scans provides an overall measure of the MT phenomenon; MTR measurements have been widely used to characterize neurologic diseases, for example, white matter lesions (11,12) and brain tumors (13,14). Recently, we reported that MTR measurements offer the potential to serve as a non-invasive biomarker of desmoplasia in PDAC (7). However, MTR, while reflecting a complex combination of the various relaxation and exchange properties, depends upon on the pulse sequence parameters such as power and offset frequency of the MT saturation pulses, flip angle (FA) of RF irradiation, repetition time (TR), etc (10,15). Consequently, characterization of the entire MT phenomenon by a simple MTR measurement may potentially overlook essential information when attempting to characterize desmoplasia in PDAC (16). Moreover, it may be difficult to compare MTR values measured with various different pulse sequence protocols and at different sites (17); the signals measured during MT MRI scans depends strongly upon the pulse sequence details and experimental conditions.

To improve the specificity of MT MRI measurements, quantitative MT (qMT) MRI methods were developed using a two-pool models to describe the bound and free populations of water in tissues (12,15,18,19). qMT MRI characterizes exchange rates of free water and macromolecular protons by modeling the saturation of the free water protons across a range of offset frequencies while accounting for the power of the MT saturation pulses and the contribution of apparent T1 relaxation rates (18). Compared to conventional MTR methods, qMT MRI provide measurements that more directly characterize the underlying properties involved in the MT process. For qMT MRI, the exchange of spin polarization between the pools of water allows calculation of fundamental parameters of the MT phenomenon, such as the bound proton fraction (BPF), the rate of MT exchange (k), and the transverse relaxation time of macromolecular spins. These parameters can change in concordance with intrinsic properties of tissues that undergo remodeling during disease progression (20,21). It has been shown that BPF—the proportion of protons that are bound to macromolecules, and the MT exchange rate (k)—the rate of exchange of magnetization between the bound and free protons, are less dependent upon specifically implemented pulse sequence details (22). qMT MRI has been widely applied for neurologic imaging studies, particularly for investigating Alzheimer disease progression (23), but qMT MRI has not been fully explored for applications in abdominal oncologic imaging.

In this study, we investigated the application of qMT MRI methods for the noninvasive quantification of fibrosis levels in PDAC. We compared BPF and k parameters extracted from the two-pool model to histologic assessments of tumor tissue fibrosis-levels in three mouse xenograft models of PDAC.

Materials and Methods

Mouse Xenograft Models

All animal studies were approved by the Animal Care and Use Committee of Northwestern University (ACUC protocol: 2010-2222). The animals were housed in isolators under standard conditions (temperature $22 \pm 2°C$, relative humidity $55 \pm 10\%$, 12 h dark/12 h light cycle) with unrestricted access to a balanced pellet diet and water conforming to institutional guidelines for the care and use of laboratory animals. The methods used for creation of the animal model were described previously (7). In short, one of the three human pancreatic cancer cell lines (Panc-1, BxPC-3, and Capan-1) obtained commercially from American Type Culture Collection (ATCC; Rockville, MD) was injected into the left and right flanks of six-week-old Balb/c nude mice (Charles River, Wilmington, MA). 21-28 days following tumor implantation mice were anesthetized with a mixture of isoflurane and oxygen (Isoflurane Vaporizer, Vaporizer Sales and Services, Rockmart, GA) for imaging.

MR Imaging

During MRI, mouse anesthesia was maintained using inhaled isoflurane 0.8-1.5% with 100% oxygen. An animal MRI compatible monitoring system (BIOPAC Systems, Inc. Goleta, CA, USA) was used for monitoring blood pulse rate, respiration rate, and temperature during imaging procedures.

MRI data were obtained using a 7 Tesla, 16 cm bore size, horizontal bore, Bruker Pharmascan coupled with a high performance BGA12-S gradient, an actively decoupled 72 mm volume coil transmitter, and a 38 mm mouse coil receiver (Bruker BioSpin, Billerica, MA). An MT sequence used for this study as described previously (7). In brief, our MT pulse sequence is a 3D spoiled gradient-echo imaging sequence (TR/TE/flip angle = 36 ms/ 2.93 ms/9°) pre-saturated by a 20 ms Gaussian pulse (peak power = 8 μT) during each TR. MT-weighted images were acquired at 11 offset frequencies to cover the logarithmic interval from 1 to 100 kHz. A 5 mm diameter NMR tube (New Era, NJ) filled with 0.3 mM $MnCl_2$ (Sigma-Aldrich, Saint Louis, MO) was placed beside the animal during the MR scans to evaluate the direct saturation effect of the MT pulse (18). B_0 and B_1 field maps were generated to correct for field variations during these MT measurements. B_1 maps were acquired using double angle methods (24). For B_0 mapping, the dual-TE GRE phase-difference method (25) was used with TR/TE1/TE2 = 36 ms/2.3 ms/2.5 ms and flip angle = 9°. T_1 relaxation data were acquired using the variable flip angle (VFA) method (26) based on the spoiled 3D GRE sequence (TR/TE = 20/2.93 ms, flip angle = 3, 10, and 20°). Additional imaging parameters included: FOV = 32×32 mm^2; slab thickness = 16 mm; 3D matrix = $128 \times 128 \times 16$; NEX = 2.

Histologic Evaluation

At the end of imaging session, mice were euthanized. The tumor xenografts were then excised and dissected. Each tumor was cut into two equal parts. One half of the tumor was stored in liquid nitrogen for biochemical analyses. The other half was fixed in 10% formalin, embedded in paraffin, and sliced (4 μm in thickness) for Masson's trichrome staining. The trichrome staining was carried out in the same batch for all the samples. To quantify the amount of fibrosis in each tumor, we measured the area of stained collagen fibers within each central tumor slice and compared this measurement to the overall tumor area.

Specifically, one central slice of these trichrome-stained slides from each tumor was scanned at 20× magnification and digitized using the TissueFAXS system (TissueGnostics, Los Angeles, CA). Next the acquired images are analyzed using HistoQuest Cell Analysis Software (TissueGnostics, Los Angeles, CA) for the automated measurement of the fibrotic tissue areas within each slide. A threshold was set (same threshold used for all samples) to segment distinct blue-stained areas for automated identification as fibrotic tissue. Necrotic tissue regions were manually excluded from these measurements. No smoothing was applied during this analysis process and there was no requirement that identified regions within these fields be connected or above a specific size to be included in the area calculation. The total tumor tissue area (A_{total}) was also measured and finally the percentage of fibrotic tissue was expressed as a ratio of the latter two area measurements: $A_{fibrosis} / A_{total} \times 100$.

MRI Data Analysis

MR image post-processing was performed offline using Matlab software (MathWorks, Natick, MA). The signal intensity from the off-resonance saturation images (M_{sat}) was normalized to that from the images without MT saturation (M_0). Using the central slice through each tumor, region of interest (ROIs) were drawn to encompass the PDAC xenograft tumor tissues while excluding areas of high signal intensity in MT-weighted images indicative of tumor necrosis (27-29). Once defined on one M_{sat} image, the ROI was then copied and applied to the corresponding M_0 and M_{sat} images at all other offset frequencies. For each ROI, the normalized signal intensities at 11 off-resonance frequencies were fit to a two-pool model of MT (12). In this model, the steady-state residual longitudinal magnetization following the MT saturation pulses is given by:

$$M_z^a = \frac{R_b\left[\frac{RM_0^b}{R_a}\right] + R_{rfb} + R_b + R}{\left[\frac{RM_0^b}{R_a}\right](R_b + R_{rfb}) + \left(1 + \left(\frac{\omega_1}{2\pi\Delta}\right)^2\left[\frac{1}{R_aT_{2a}}\right]\right)(R_b + R_{rfb} + R)} \quad (1)$$

where M^a_z, the z component of the magnetization of the free protons (pool A), is the normalized signal intensity. M^b_0 is the magnetization of the protons bound to macromolecular pool (pool B).   is the frequency offset of the MT saturation pulse. R is a constant representing the exchange rate between the two pools. R_a and R_b are the longitudinal relaxation rates for pool A and pool B respectively. R_{rfa} and R_{rfb} can be considered the rate of saturation of the longitudinal magnetization of pool A and pool B due to the offset RF irradiation. For a macromolecular pool in biological tissues, a super Lorentzian line shape is generally considered suitable to characterize the experimental MT data when using the two-pool model (30). R_{rfa} and R_{rfb} are expressed as

$$R_{rfa} = \frac{\omega_1^2 T_{2a}}{1 + (2\pi\Delta T_{2a})^2} \quad (2)$$

$$R_{rfb} = \omega_1^2 \pi g(2\pi\Delta) \quad (3)$$

where

$$g(2\pi\Delta) = \int_0^{\frac{\pi}{2}} d\theta \sin\theta \sqrt{\frac{\pi}{2}} \frac{T_{2b}}{|3\cos^2\theta - 1|} e^{-2\left[\frac{2\pi\Delta T_{2b}}{3\cos^2\theta - 1}\right]^2} \quad (4)$$

T_{2a} and T_{2b} are the transverse relaxation times of pool A and pool B respectively. $_1$ is the angular frequency of the off-resonance saturating RF pulse and is a measure of the

amplitude of the saturating RF field (18). For Gaussian pulse used in this study, ω_1 is expressed as

$$\omega_1 = \gamma B_{1CWPE} \quad (5)$$

where B_{1CWPE} is the equivalent continuous wave RF field of the Gaussian pulse during one TR(12).

When experimental MT data was fit to Eq. 1, five model parameters (R_b, T_{2b}, R, $[RM_0^b/R_a]$, and $[1/R_aT_{2a}]$) were determined. R_a was determined separately by the following equation:

$$R_a = \frac{R_a^{obs}}{1 + \left[\frac{M_0^b}{R_a}\right](R_b - R_a^{obs})} \quad (6)$$

where R_a^{obs} is the longitudinal relaxation rate ($R_a^{obs} = 1/T_1$) independently measured (using the VFA method in this study) (18). [M0b/Ra], as a whole, is determined by R and [RM0b/Ra] that are extracted from Eq.1. R_b was fixed arbitrarily to be 1 s^{-1} for all tissue types since this qMT model is insensitive to R_b (15,30-32). A trust-region-reflective algorithm was used for the data fitting process (33,34). The mean squared residuals of the data fitting were less than 0.005.

Bound proton fraction (BPF) was defined as $100 \times M_0^b/(M_0^b + M_0^a)$, where $M_0^a = 1$, and M_0^b is determined by the fitted R, $[RM_0^b/R_a]$, and independently measured R_a from Eq. 6. MT exchange rate (k) in this model equals to $[RM_0^b]$.

MTR was calculated for the 3500 Hz offset frequency as follows: $100 \times (1 - M_{sat}/M_0)$, where M_{sat} represents the signal intensity for image acquired following application of the MT pulse, M_0 is the signal intensity image acquired without MT saturation, i.e. RF saturation pulses applied at 100 kHz.

Statistical Analysis

For each MR image, we calculated the mean BPF, MT exchange rate (k), and MTR across all ROIs. Both the MRI data and histologic data are expressed as means ± standard deviations (SD). For either MRI or histologic data, one way analysis of variance (ANOVA) was applied to compare means measured for tumors produced from the three different PDAC cell lines. Bartlett's test was performed for equal variances and Scheffe method for post-hoc testing. Pearson correlation coefficients were calculated to assess the linear relationship between each of the qMT MRI parameters and corresponding histologic fibrosis measurements. All statistical analyses were performed with Stata software (Stata11, Stata-Corp, College Station, Tex). Statistical significance was defined as $P < 0.05$.

Results

Eighteen PDAC xenografts were grown with 6 tumors from each of Panc-1, BxPC-3 and Capan-1 cell lines. Tumor size ranges from 4 to 8 mm in diameter. Fig. 1a shows a representative nude mouse with tumors in left and right flanks. Typical MT weighted images and qMT MRI maps are shown in Fig. 1c, d, e and f. The tumor on the right flank was grown from BxPC-3 cell line and had measurably lower signal intensity ($(1.02 \pm 0.16) \times 10^4$, mean ± SD, arbitrary unit (AU)) in MT-weighted images compared to the tumor in the left flank ($(1.19 \pm 0.24) \times 10^4$, AU) that was grown from Panc-1 cell line (Fig. 1c), though no such significant difference ($(1.76 \pm 0.22) \times 10^4$ AU and $(1.78 \pm 0.31) \times 10^4$ AU for

BxPC-3 and Panc-1 tumor respectively) was observed for image without MT pulse (Fig. 1b). MTR values for the BxPC-3 tumor (41.95 ± 3.06, mean ± SD) were higher than the MTR values for the Panc-1 tumor (32.99 ± 2.12) (Fig. 1d). BPF map (Fig. 1e) shows that the BxPC-3 tumor had higher BPF values (4.50 ± 0.25) compared to BPF values for the Panc-1 tumor (3.82 ± 0.23) with a similar trend observed in the k map (Fig 1f).

Group average of normalized MT signal for three tumor types are shown in Fig. 2a. MT data and fitting results from a representative experiment are shown in Fig. 2b; these model fits include MT data collected at 11 different offset frequencies. While Bartlett's test indicated that populations of the measured parameters all had the same standard deviation with the P values greater than 0.21, a significant difference was found between BPFs of BxPC-3, Panc-1 and Capan-1 xenografts (one way ANOVA, F = 49.93, $P < 0.01$). As shown in Fig. 4, Scheffe test indicated that the mean BPF of the tumors grown from BxPC-3 cell line (mean BPF, 5.31 ± 0.87) was significantly higher than that of tumors grown from Panc-1 (mean BPF, 3.65 ± 0.60) and Capan-1 (mean BPF, 1.50 ± 0.58) cell lines ($P < 0.01$ respectively). Post hoc Scheffe test showed that the mean cross relaxation rates (k) of the tumors from BxPC-3 (mean k, 5.98 ± 2.43) and Panc-1 (mean k, 6.96 ± 1.93) cell lines were both significantly higher than that of Capan-1 tumors (mean k, 1.50 ± 1.34) ($P < 0.01$ respectively), though no significant difference was found for between k values of BxPC-3 tumors and k values for Panc-1 tumors ($P = 0.69$). The mean MTR of the tumors from BxPC-3 (mean MTR, 36.94 ± 5.40) was significantly higher than that of tumors grown from Capan-1 (mean MTR, 28.14 ± 4.86, $P = 0.01$) cell line, while the MTR of Panc-1 tumors (mean MTR, 31.82 ± 2.57) showed no significant difference from BxPC-3 ($P = 0.17$) and Capan-1 ($P = 0.38$) tumors, respectively.

As indicated in the trichrome staining slides (Fig. 3), tumors grown from BxPC-3 cells developed thick fibrotic stoma, which was seen histologically as bands of collagen surrounding tumor cells throughout the xenografts (Fig. 3a). Tumors grown from Panc-1 and Capan-1 cell lines appeared much less fibrosis (Fig. 3b and c respectively). The area percentages of collagen fiber of tumors measured from trichrome-stained slides are shown in Fig. 4d. Tumors grown from BxPC-3 cell line had significantly higher fibrosis areas (mean area percentage, 6.21 ± 2.10) than Panc-1 (2.88 ± 1.13) and Capan-1 (1.69 ± 1.01) tumors, respectively. One way ANOVA post hoc Scheffe test showed a significant difference between fibrosis levels in BxPC-3 xenografts and Panc-1 xenografts ($P < 0.01$) and between BxPC-3 and Capan-1 xenografts ($P < 0.01$), while no significant difference was found between fibrotic areas in Panc-1 and Capan-1 xenografts ($P = 0.41$). BPF measurements demonstrated a correlation with the quantity of PDAC tumor fibrosis (18 tumors; R = 0.77, $P < 0.01$; Fig 5a) while only a moderate correlation (18 tumors; R = 0.59, $P < 0.01$; Fig 5c) was observed between MTR and fibrotic area and a poor correlation (18 tumors; R = 0.38, $P = 0.12$; Fig 5b) between k and the tumor fibrotic area.

Discussion

In the current study, we performed two-pool model based quantitative magnetic transfer MRI measurements in three mouse xenograft models of PDAC. We found that these qMT MRI measurements were significantly different between xenograft tumors developed from the three PDAC cell lines. These imaging findings were well correlated to histologically assessed desmoplastic fibrosis levels. The qMT MRI parameter — bound proton fraction (BPF) — demonstrated a strong correlation to fibrosis levels. Our results indicate that qMT MRI measurements may serve to identify and quantify desmoplasia *in vivo* in the setting of pancreatic cancer.

MT is a dynamic physical process that can probe subpopulations of water protons in cells and tissues that are bound to macromolecules. Thus, MT MRI generates contrast that is primarily determined by the fraction of large macromolecules or immobilized phospholipid cell membranes within the interrogated tissue (8,10). In our previous study, we demonstrated that MTR measurements were higher in xenograft tumors generated from the BxPC-3 cell line than tumors generated from Panc-1 and Capan-1 (7) cell lines. The latter results suggested the feasibility of using MTR measurements as a noninvasive biomarker of tumor associated desmoplasia in PDAC. However, in practice, it is possible that identical semi-quantitative MTR values could be measured in two very dissimilar tissues as a consequence of the sub-optimal selection of pulse sequence parameters, even if the actual magnetization exchange rates in these tissues is quite different (16). Alternatively, qMT MRI parameters, derived from a model characterizing all of the relaxation and exchange rates of the free water and macromolecular protons, should more reliably change in concordance with the intrinsic properties of the tissue. In PDAC, alterations in BPF, one of the qMT MRI parameters measured in this study, should be closely related to changes in the ratio of collagen to water content due to effective magnetization transfer between collagen and water. Measurement of the BPF also has the advantage of being relatively insensitive to the precise details of the MR experiment, including tissue orientation relative to the main B_o field and field strength (35,36). In the current study, we found that BPF for skeletal muscle was 10.35 ± 1.73 percent comparable to prior reports of 7.4 ± 1.3 percent at 3T (35) and 6.9 ± 1.6 percent at 1.5 T (37). We found that BPF was higher in tumors generated from the BxPC-3 cell line (5.31 ± 0.87) than the Panc-1 (3.65 ± 0.60) and Capan-1 (1.50 ± 0.58) cell lines. These findings were consistent with histologic trichrome measurements of mean fibrotic area in the corresponding xenograft tissue samples. MTR measurements were also well correlated with fibrosis levels (Fig. 5c), confirming our findings in a previous report (7).

Several limitations existed in this study. First, qMT MRI measurements require extensive data processing and scan time. Multiple scans with a range of offset frequencies for the MT pulses are required to extract the qMT MRI parameters. The long imaging time could lead to image artifacts due to patient motion in clinical settings. However, the drawback of long acquisition times for qMT MRI could potentially be solved by the use of more recently developed MT-sensitized methods using balanced steady state free precession (38) and additionally developed analysis methods for rapid quantitative mapping of macromolecular proton fractions (39). Second, xenograft models with subcutaneous tumors rather than transgenic models or clinical patients with in situ pancreatic disease were investigated in this study. However, these xenograft models and associated cell lines have been highly valuable for prior studies of PDAC desmoplasia (2,40,41) thus we anticipate that our qMT methods will remain effective for assessing fibrosis within pancreatic tumors. Further translational validation studies remain necessary. In addition, different pancreatic cancer etiologies may have different total protein content, which could give rise to different MT-MRI contrast. Future clinical studies could be valuable to evaluate the relationship between qMT MRI measurements and histologic tumor protein content. Third, the current study was performed with ROI-based measurements that encompassed the entire tumor within each slice for both MRI and histology measurements. The latter approach mitigates difficulties associated with the co-registration of histology slides to corresponding in vivo MRI measurements. However, additional studies may be valuable to investigate the potential to use qMT MRI methods to further probe the intra-tumoral heterogeneity of collagen deposition and to differentiate tumor necrosis. Great care was taken to extract a tumor pathology sample at the center of each tumor for comparison to the central tumor MR imaging slice. Nonetheless, inherent imprecision associated with this manual orientation and slicing process along with the significant difference between MRI slice thickness (1.0 mm) and histology tissue slice thickness (4 μm) may have been a key source of variability between the MRI and histologic

measurements within individual animal. Future studies using multi-slice whole tumor measurements and biochemical whole tumor collagen measurements with western blot (42) and/or enzyme-linked immunosorbent assays (43) could be particularly valuable. Finally, it should be noted that 11 data points were used in this study to fit the five free parameters in Eq.1. Uncertainties in fitted parameters are possible (i.e. an equally good fit could conceivably be obtained with different combinations of parameter values). To minimize the fitting uncertainties, upper and lower bounds for a particular parameter could be set according to prior knowledge. Clearly additional future studies are warranted to carefully consider optimal fitting approaches as well as the most accurate and efficient models for fitting these qMT datasets (36).

In conclusion, we have demonstrated that qMT MRI can depict desmoplastic stoma in subcutaneous xenograft mouse tumor models of PDAC. Our results indicated that qMT measurements offer the potential to noninvasively quantify fibrosis levels in PDAC mouse xenograft models and thus serve as a valuable *in vivo* biomarker of desmoplasia in PDAC.

Acknowledgments

Supply a list of abbreviations used, excluding standard abbreviations

PDAC	pancreatic ductal adenocarcinoma
MT	magnetization transfer
MTR	magnetization transfer ratio
qMT	quantitative magnetization transfer
BPF	bound proton fraction
ROI	region of interest
FA	flip angle
ATCC	American Type Culture Collection
ANOVA	one way analysis of variance
SD	standard deviations
AU	arbitrary unit

References

1. Jemal A, Siegel R, Ward E, Hao Y, Xu J, Murray T, Thun MJ. Cancer Statistics, 2008. CA Cancer J Clin. 2008; 58(2):71–96. [PubMed: 18287387]

2. Olive KP, Jacobetz MA, Davidson CJ, Gopinathan A, McIntyre D, Honess D, Madhu B, Goldgraben MA, Caldwell ME, Allard D, Frese KK, DeNicola G, Feig C, Combs C, Winter SP, Ireland-Zecchini H, Reichelt S, Howat WJ, Chang A, Dhara M, Wang L, Ruckert F, Grutzmann R, Pilarsky C, Izeradjene K, Hingorani SR, Huang P, Davies SE, Plunkett W, Egorin M, Hruban RH, Whitebread N, McGovern K, Adams J, Iacobuzio-Donahue C, Griffiths J, Tuveson DA. Inhibition of Hedgehog Signaling Enhances Delivery of Chemotherapy in a Mouse Model of Pancreatic Cancer. Science. 2009; 324(5933):1457–1461. [PubMed: 19460966]

3. Muraoka N, Uematsu H, Kimura H, Imamura Y, Fujiwara Y, Murakami M, Yamaguchi A, Itoh H. Apparent diffusion coefficient in pancreatic cancer: Characterization and histopathological correlations. Journal of Magnetic Resonance Imaging. 2008; 27(6):1302–1308. [PubMed: 18504750]

4. Wang Y, Chen ZE, Nikolaidis P, McCarthy RJ, Merrick L, Sternick LA, Horowitz JM, Yaghmai V, Miller FH. Diffusion-weighted magnetic resonance imaging of pancreatic adenocarcinomas: Association with histopathology and tumor grade. Journal of Magnetic Resonance Imaging. 2011; 33(1):136–142. [PubMed: 21182131]

5. Fattahi R, Balci NC, Perman WH, Hsueh EC, Alkaade S, Havlioglu N, Burton FR. Pancreatic Diffusion-Weighted Imaging (DWI): Comparison Between Mass-Forming Focal Pancreatitis (FP), Pancreatic Cancer (PC), and Normal Pancreas. Journal of Magnetic Resonance Imaging. 2009; 29(2):350–356. [PubMed: 19161187]

6. Bali MA, Metens T, Denolin V, Delhaye M, Demetter P, Closset J, Matos C. Tumoral and Nontumoral Pancreas: Correlation between Quantitative Dynamic Contrast-enhanced MR Imaging and Histopathologic Parameters. Radiology. 2011; 261(2):456–466. [PubMed: 21852570]

7. Li W, Zhang Z, Nicolai J, Yang GY, Omary RA, Larson AC. Magnetization transfer MRI in pancreatic cancer xenograft models. Magn Reson Med. 2012; 68(4):1291–1297. [PubMed: 22213176]

8. Wolff SD, Balaban RS. Magnetization transfer contrast (MTC) and tissue water proton relaxation in vivo. Magn Reson Med. 1989; 10(1):135–144. [PubMed: 2547135]

9. Wolff SD, Balaban RS. Magnetization transfer imaging: practical aspects and clinical applications. Radiology. 1994; 192(3):593–599. [PubMed: 8058919]

10. Henkelman RM, Stanisz GJ, Graham SJ. Magnetization transfer in MRI: a review. NMR Biomed. 2001; 14(2):57–64. [PubMed: 11320533]

11. Kucharczyk W, Macdonald PM, Stanisz GJ, Henkelman RM. Relaxivity and magnetization transfer of white matter lipids at MR imaging: importance of cerebrosides and pH. Radiology. 1994; 192(2):521–529. [PubMed: 8029426]

12. Ramani A, Dalton C, Miller DH, Tofts PS, Barker GJ. Precise estimate of fundamental in-vivo MT parameters in human brain in clinically feasible times. Magn Reson Imaging. 2002; 20(10):721–731. [PubMed: 12591568]

13. Kurki T, Niemi P, Valtonen S. MR of intracranial tumors: combined use of gadolinium and magnetization transfer. AJNR Am J Neuroradiol. 1994; 15(9):1727–1736. [PubMed: 7847221]

14. Okumura A, Takenaka K, Nishimura Y, Asano Y, Sakai N, Kuwata K, Era S. The characterization of human brain tumor using magnetization transfer technique in magnetic resonance imaging. Neurol Res. 1999; 21(3):250–254. [PubMed: 10319332]

15. Sled JG, Pike GB. Quantitative imaging of magnetization transfer exchange and relaxation properties in vivo using MRI. Magn Reson Med. 2001; 46(5):923–931. [PubMed: 11675644]

16. Garcia M, Gloor M, Radue EW, Stippich C, Wetzel SG, Scheffler K, Bieri O. Fast high-resolution brain imaging with balanced SSFP: Interpretation of quantitative magnetization transfer towards simple MTR. Neuroimage. 2012; 59(1):202–211. [PubMed: 21820061]

17. Berry I, Barker GJ, Barkhof F, Campi A, Dousset V, Franconi J-M, Gass A, Schreiber W, Miller DH, Tofts PS. A multicenter measurement of magnetization transfer ratio in normal white matter. Journal of Magnetic Resonance Imaging. 1999; 9(3):441–446. [PubMed: 10194715]

18. Henkelman RM, Huang X, Xiang QS, Stanisz GJ, Swanson SD, Bronskill MJ. Quantitative interpretation of magnetization transfer. Magn Reson Med. 1993; 29(6):759–766. [PubMed: 8350718]

19. Yarnykh VL. Pulsed Z-spectroscopic imaging of cross-relaxation parameters in tissues for human MRI: theory and clinical applications. Magn Reson Med. 2002; 47(5):929–939. [PubMed: 11979572]

20. Li W, Hong L, Hu L, Magin RL. Magnetization Transfer Imaging Provides a Quantitative Measure of Chondrogenic Differentiation and Tissue Development. Tissue Eng Part C Methods. 2010

21. Lee RR, Dagher AP. Low power method for estimating the magnetization transfer bound-pool macromolecular fraction. Journal of Magnetic Resonance Imaging. 1997; 7(5):913–917. [PubMed: 9307919]

22. Cercignani M, Barker GJ. A comparison between equations describing in vivo MT: The effects of noise and sequence parameters. J Magn Reson. 2007

23. Ridha BH, Tozer DJ, Symms MR, Stockton KC, Lewis EB, Siddique MM, MacManus DG, Rossor MN, Fox NC, Tofts PS. Quantitative magnetization transfer imaging in Alzheimer disease. Radiology. 2007; 244(3):832–837. [PubMed: 17709831]

24. Wang D, Zuehlsdorff S, Larson AC. Rapid 3D radiofrequency field mapping using catalyzed double-angle method. NMR in Biomedicine. 2009; 22(8):882–890. [PubMed: 19492303]

25. Skinner TE, Glover GH. An extended two-point Dixon algorithm for calculating separate water, fat, and B0 images. Magn Reson Med. 1997; 37(4):628–630. [PubMed: 9094088]

26. Fram EK, Herfkens RJ, Johnson GA, Glover GH, Karis JP, Shimakawa A, Perkins TG, Pelc NJ. Rapid calculation of T1 using variable flip angle gradient refocused imaging. Magn Reson Imaging. 1987; 5(3):201–208. [PubMed: 3626789]

27. Tseng JR, Kang KW, Dandekar M, Yaghoubi S, Lee JH, Christensen JG, Muir S, Vincent PW, Michaud NR, Gambhir SS. Preclinical Efficacy of the c-Met Inhibitor CE-355621 in a U87 MG Mouse Xenograft Model Evaluated by 18F-FDG Small-Animal PET. Journal of Nuclear Medicine. 2008; 49(1):129–134. [PubMed: 18077531]

28. Koch MR, Jagannathan JP, Shinagare AB, Krajewski KM, Raut CP, Hornick JL, Ramaiya NH. Imaging features of primary anorectal gastrointestinal stromal tumors with clinical and pathologic correlation. Cancer Imaging. 2013; 12:557–565. [PubMed: 23400107]

29. Santamaria G, Velasco M, Bargallo X, Caparros X, Farrus B, Luis Fernandez P. Radiologic and pathologic findings in breast tumors with high signal intensity on T2-weighted MR images. Radiographics. 2010; 30(2):533–548. [PubMed: 20228333]

30. Morrison C, Henkelman RM. A model for magnetization transfer in tissues. Magn Reson Med. 1995; 33(4):475–482. [PubMed: 7776877]

31. Yarnykh VL, Yuan C. Cross-relaxation imaging reveals detailed anatomy of white matter fiber tracts in the human brain. Neuroimage. 2004; 23(1):409–424. [PubMed: 15325389]

32. Underhill HR, Yuan C, Yarnykh VL. Direct quantitative comparison between cross-relaxation imaging and diffusion tensor imaging of the human brain at 3.0 tesla. Neuroimage. 2009; 12:12.

33. Coleman TF, Li Y. On the convergence of interior-reflective Newton methods for nonlinear minimization subject to bounds. Mathematical Programming. 1994; 67(1):189–224.

34. Coleman TF, Li Y. An Interior Trust Region Approach for Nonlinear Minimization Subject to Bounds. SIAM Journal on Optimization. 1996; 6(2):418–445.

35. Stanisz GJ, Odrobina EE, Pun J, Escaravage M, Graham SJ, Bronskill MJ, Henkelman RM. T1, T2 relaxation and magnetization transfer in tissue at 3T. Magn Reson Med. 2005; 54(3):507–512. [PubMed: 16086319]

36. Portnoy S, Stanisz GJ. Modeling pulsed magnetization transfer. Magn Reson Med. 2007; 58(1): 144–155. [PubMed: 17659607]

37. Graham SJ, Stanisz GJ, Kecojevic A, Bronskill MJ, Henkelman RM. Analysis of changes in MR properties of tissues after heat treatment. Magnetic Resonance in Medicine. 1999; 42(6):1061–1071. [PubMed: 10571927]

38. Bieri O, Mamisch TC, Trattnig S, Scheffler K. Steady state free precession magnetization transfer imaging. Magn Reson Med. 2008; 60(5):1261–1266. [PubMed: 18956423]

39. Yarnykh VL. Fast macromolecular proton fraction mapping from a single off-resonance magnetization transfer measurement. Magnetic Resonance in Medicine. 2011 n/a-n/a.

40. Bailey JM, Swanson BJ, Hamada T, Eggers JP, Singh PK, Caffery T, Ouellette MM, Hollingsworth MA. Sonic Hedgehog Promotes Desmoplasia in Pancreatic Cancer. Clinical Cancer Research. 2008; 14(19):5995–6004. [PubMed: 18829478]

41. Dangi-Garimella S, Krantz SB, Barron MR, Shields MA, Heiferman MJ, Grippo PJ, Bentrem DJ, Munshi HG. Three-Dimensional Collagen I Promotes Gemcitabine Resistance in Pancreatic Cancer through MT1-MMP–Mediated Expression of HMGA2. Cancer Res. 2011; 71(3):1019–1028. [PubMed: 21148071]

42. Adler J, Swanson SD, Schmiedlin-Ren P, Higgins PDR, Golembeski CP, Polydorides AD, McKenna BJ, Hussain HK, Verrot TM, Zimmermann EM. Magnetization Transfer Helps Detect Intestinal Fibrosis in an Animal Model of Crohn Disease. Radiology. 2011; 259(1):127–135. [PubMed: 21324841]

43. Lequin RM. Enzyme Immunoassay (EIA)/Enzyme-Linked Immunosorbent Assay (ELISA). Clin Chem. 2005; 51(12):2415–2418. [PubMed: 16179424]
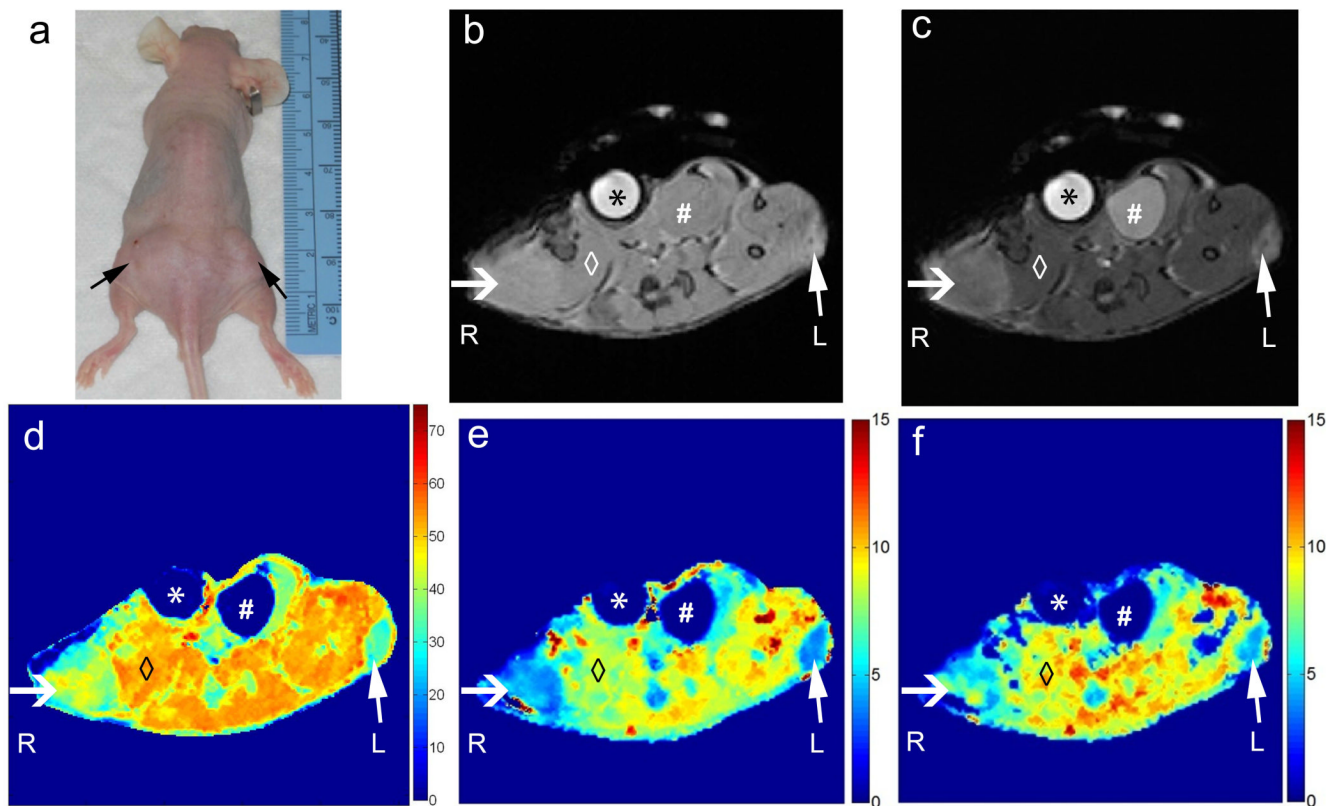
Figure 1.
An example of PDAC xenograft tumors and corresponding MR images and MT maps. (**a**) xenografts (black arrows) grown using PDAC cell lines injected subcutaneously in mouse flanks. The tumor in the left flank was grown from Panc-1 cell line and the tumor in the right flank was grown from BxPC-3 cell line. (**b**) Axial MR image without MT saturation acquired using a 3D GRE sequence (RF saturation pulses applied at 100 kHz). (**c**) Axial MR image of the same slice with MT saturation applied 3.5 kHz off-resonance using same sequence. (**d**) MTR map. (**e**) bound proton fraction (BPF) map. (**f**) MT exchange rate map. For this representative mouse, as indicated in d), e) and f), the BxPC-3 tumor (white open arrows) on the right flank demonstrated higher MT effects compared to the left flank Panc-1 tumor (white close arrows). While $MnCl_2$ (*) and urine (#) showed little MT effect, strong MT effects were demonstrated in skeletal muscle ( ). "L" and "R" indicate the anatomic left and right sides of the mouse respectively.
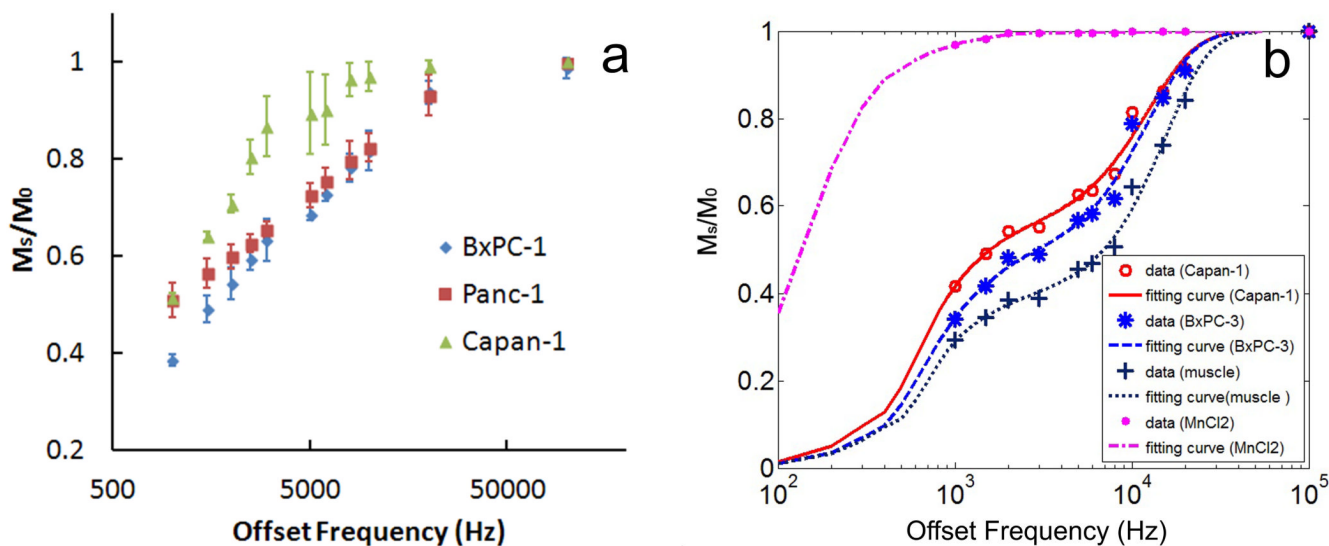
Figure 2.
a) Group average of normalized MT signal for three xenograft tumor types at 11 offset frequencies and b) representative MT curves for tumors grown from Capan-1 and BxPC-3 cells. Lines represent model fits to the collected MRI data. A trust-region-reflective algorithm was used for the data fitting process. The mean squared residuals following data fitting were less than 0.005 for each curve. Curves fitted from data sampled from $MnCl_2$ solution and skeletal muscle are also shown.
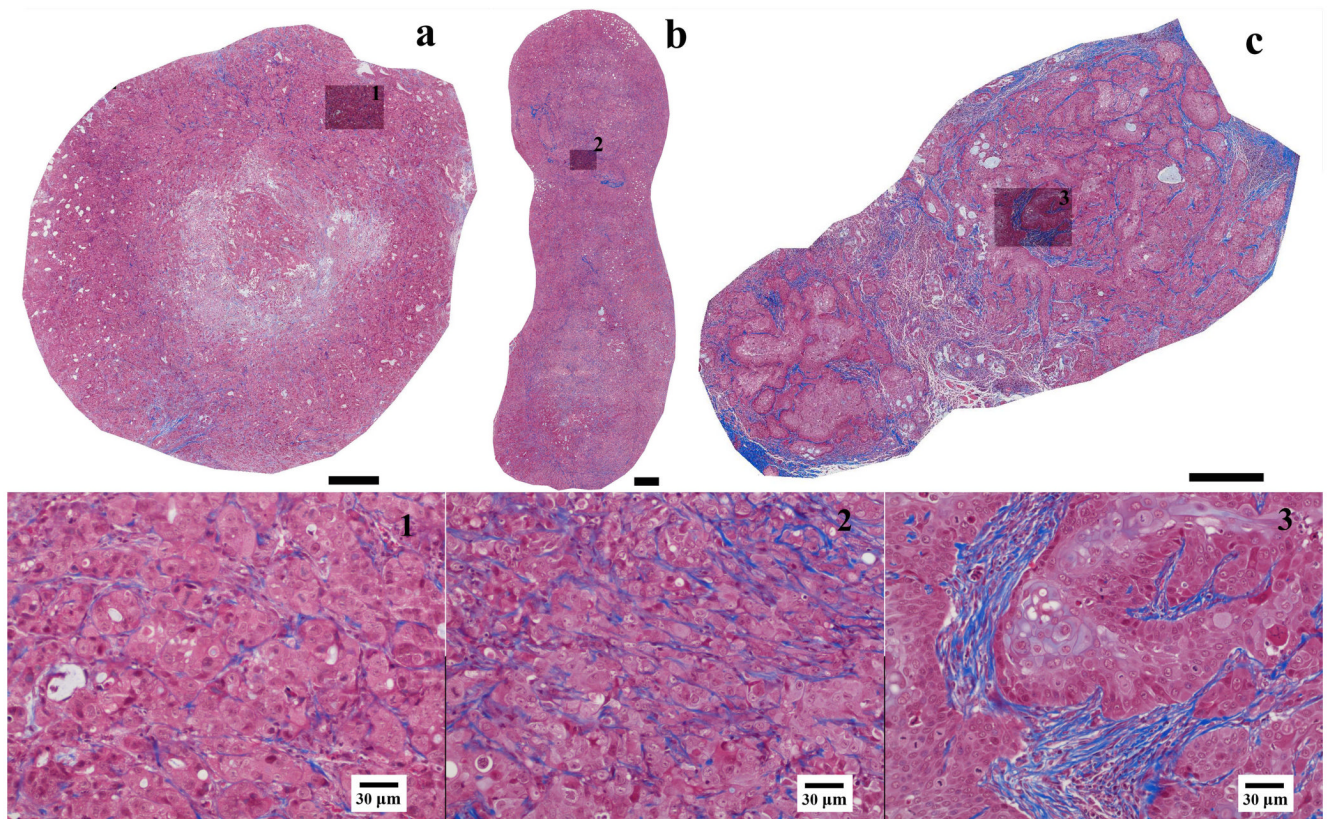
Figure 3.
Masson-trichrome stained histology slices from tumors grown using each of the three PDAC cell lines: (a) Capan-1, (b) Panc-1 and (c) BxPC-3. Top panel depicts the lower power image of each tumor (scale bar: 0.5 mm) showing the overall distribution of fibrotic tissue within these central tumor slices; lower panel shows the high power images of the inset positions 1-3 (shaded boxes) from the lower power images. Fibrotic stroma is depicted as blue-stained bands of collagen. These images demonstrate the different levels of fibrosis and associated collagen deposition within tumors.
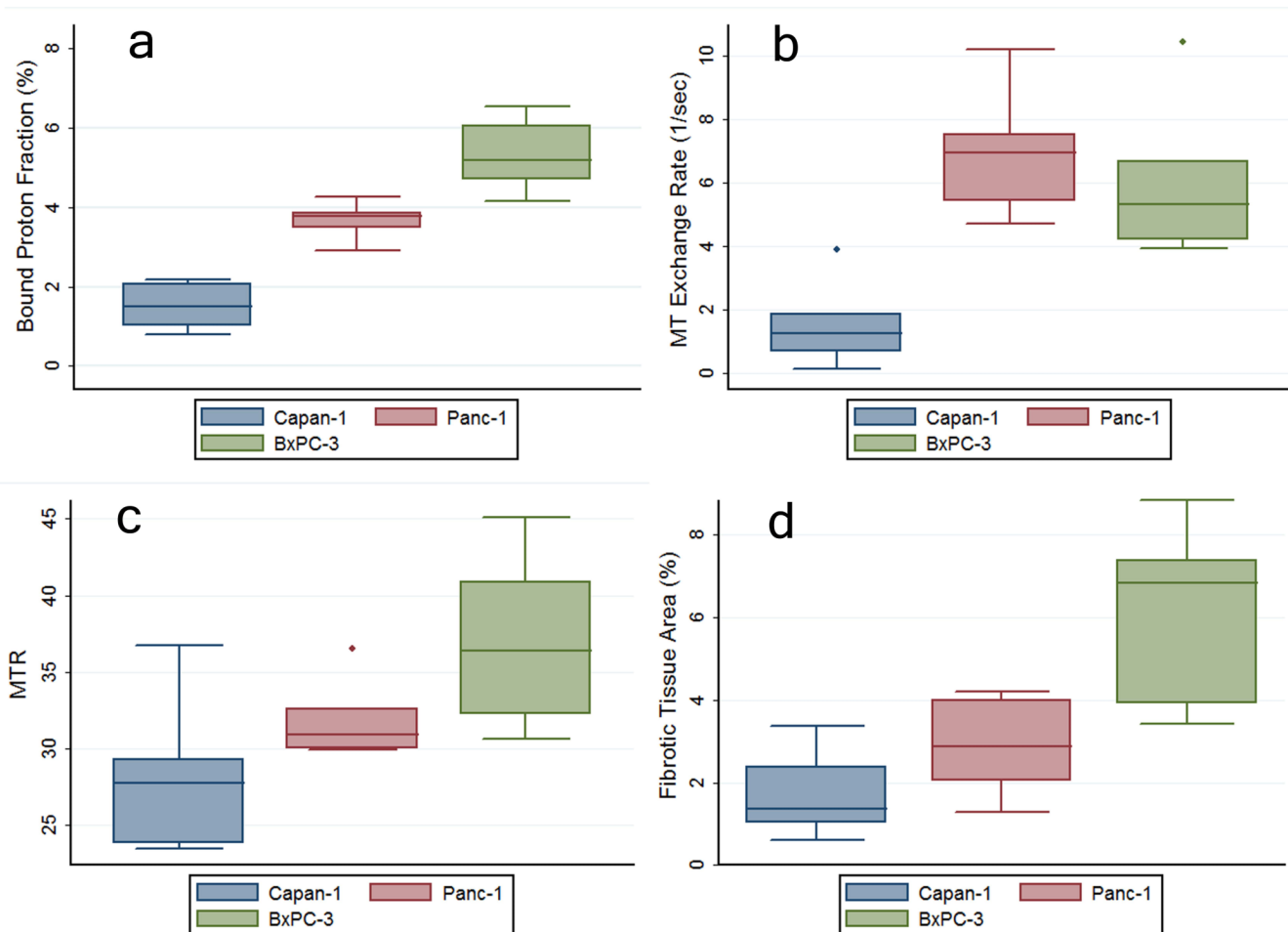
Figure 4.
Box-and-Whisker plots for bound proton fraction (**a**), MT exchange rate (**b**), MTR (**c**), and histologic fibrotic tissue area measurements (**d**) for each of the three cell lines: Capan-1, Panc-1 and BxPC-3. The horizontal line in the box interior represents the mean value. The length of the box represents the interquartile range (the distance between the 25th and the 75th percentiles). The whiskers represent extreme data from the 10th to 90th percentiles. Any further outliers are represented by separate dots.
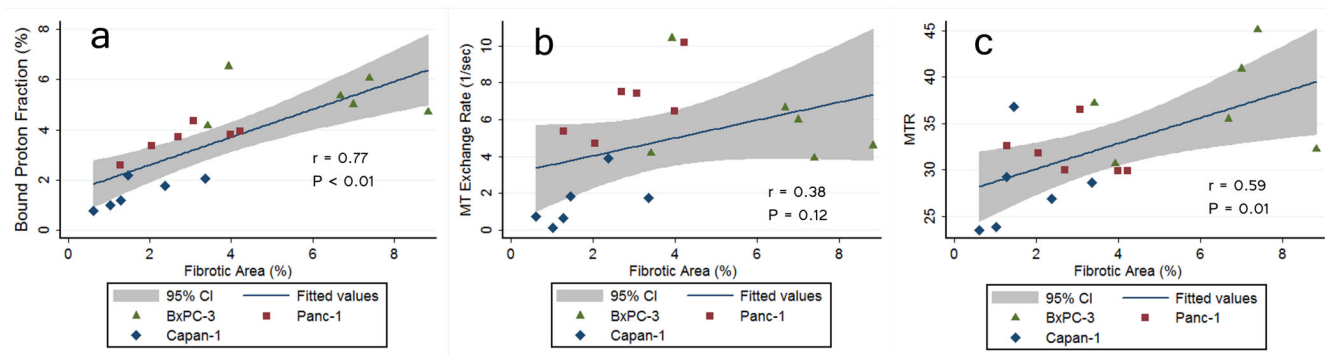
Figure 5.
Graphs showing the relationship between histologic fibrotic tissue area measurements and bound proton fraction (a), MT exchange rate (b) and MTR (c) for tumors grown from the three cell lines: Capan-1 (n = 6), Panc-1 (n = 6), and BxPC-3 (n = 6). The shaded region represents the 95% confidence interval for linear regression of fibrosis on qMT MRI and MTR measurements.